Nuclear Materials and Energy 43 (2025) 101941

Contents lists available at ScienceDirect

Nuclear Materials and Energy

journal homepage: www.elsevier.com/locate/nme

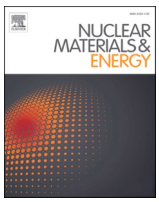

Balmer emission measurements in JET-ILW hydrogen, deuterium, tritium and deuterium-tritium low-confinement mode plasmas☆,☆

A.G. Meigs [a,*], M. Groth [b], V.-P. Rikala [b], B. Lomanowski [c], N. Vianello [d], M. Wischmeier [e], the JET contributors[1]

[a] UKAEA, Culham Campus, Abingdon, Oxfordshire OX14 3DB, UK
[b] Aalto University, Espoo, Finland
[c] Oak Ridge National Laboratory, Oak Ridge, TN, USA
[d] Consorzio RFX, CNR, ENEA, INFN, Universita di Padova, Padova, Italy
[e] Max Planck Institut fur Plamaphysik, Garching, Germany

ARTICLE INFO

Keywords:
JET
Divertor
Balmer
Detachment
Density limit
Spectroscopy
DT
T

ABSTRACT

Measurements of Balmer-alpha (B-α) and Balmer-gamma (B-γ), where B = H, D, or T isotopes of hydrogen, emission across the low-field side (LFS) divertor in JET ITER-like Wall (ILW), low-confinement mode (L-mode) plasma indicate that the divertor plasma was more strongly detached in deuterium, tritium and deuterium–-tritium than in hydrogen plasmas. These measurements are consistent with the lower degree of detachment in hydrogen versus tritium plasmas inferred from Langmuir probes (Groth et al., 2023) [1]. The ratio of B-γ to B-α is a suitable indicator of high density/low temperature conditions because B-α emission is dominated by electron impact excitation with a small electron–ion recombination component regardless of electron temperature and density (for conditions in tokamak plasmas) whilst for B-γ the recombination component increases and the excitation component decreases as the electron temperature decreases and the electron density increases. Within the uncertainty of the measurements, the electron density at the low-field side separatrix and the power crossing the separatrix are similar to permit these comparisons. The B-©/B-α ratio is well correlated with the onset of detachment as measured by Langmuir probes (McCracken et al., 1998; Groth et al., 2023). The ratios of B-γ and B-α varied between 0.005 and 0.035 for low-recycling, high-recycling and partially detached conditions, and were 60–70 % higher in partially detached hydrogen than in tritium plasmas. In contrast, the difference between deuterium, tritium and 40–60 % deuterium–tritium is within 10 % and thus within the uncertainties of the measurements. Profiles of the B-α and B-γ emission was measured with two filtered CCDs connected to the visible lost light leg of JET's mirror link spectroscopy system (Meigs et al., 2010; Lomanowski et al., 2014)[4,5]. Spatially (radial) narrower B-α profiles were measured with increasing isotope mass, while similarly broadened B-γ profiles were measured.

☆ JET, which was previously a European facility, is now a UK facility collectively used by all European fusion laboratories under the EUROfusion consortium. It is operated by the United Kingdom Atomic Energy Authority, supported by DESNZ and its European partners. This work, which has been carried out within the framework of the Contract for the Operation of the JET Facilities up to 31 October 2021, has been funded by the Euratom Research and Training Programme. Since 31 October 2021, UKAEA has continued to work with the EUROfusion Consortium as an Associated Partner of Max-Plank-Gesellschaft zur Förderung der Wissenschafte.V represented by Max-Plank-Institut fur Plasmaphysik ("IPP") pursuant to Article 9.1 of the EUROfusion Grant Agreement for Project No 101052200. The views and opinions expressed herein do not necessarily reflect those of the European Commission.

☆ This article is part of a special issue entitled: 'PSI-26' published in Nuclear Materials and Energy.

* Corresponding author.
E-mail address: Andrew.Meigs@ukaea.uk (A.G. Meigs).

[1] See the author list of "Overview of T and D-T results in JET with ITER-like wall" by CF Maggi et al. to be published in Nuclear Fusion Special Issue: Overview and Summary Papers from the 29th Fusion Energy Conference (London, UK, 16-21 October 2023).

https://doi.org/10.1016/j.nme.2025.101941
Received 4 July 2024; Received in revised form 18 April 2025; Accepted 19 April 2025
Available online 21 April 2025

Introduction

Detached divertor operations are necessary to reduce heat flux to the divertor target plates [6]. This regime is obtained by two primary methods: impurity gas injection into the divertor or operations near the so-called density limit using hydrogenic gas puffing. This paper is concerned with the second method. Over the last 12 years, during ITER-like Wall (ILW) program of JET, a study of L-mode operation with density limit ramps and stepped discharges was performed in all the isotopes of hydrogen (protium: H, deuterium: D, tritium: T) with varying divertor pump conditions (supercritical helium pumped divertor, sc-He, and liquid nitrogen cooled nearly unpumped, LN2) and a variety of gas injection systems (faster rate, el/s, of injection in sc-He due to the increased pumping efficiency, versus slower LN2 where the pumping efficiency is much lower). This paper investigates the behaviour of detachment in density ramp discharges from primarily the point of view of hydrogenic Balmer spectroscopy (intensity and Stark broadening for line-of-sight averaged divertor, LOS-avg, electron density) and the bremsstrahlung continuum above and below the Balmer decrement (LOS-avg electron temperature). The discharges were nominally operated at a toroidal field of 2.5 T and a plasma current of 2.5 MA with neutral beam heating of 1.0 MW with a density ramp over 10–16 s (varying ramp rate) and a significant variation in fuelling rates due to the difference in pumping of sc-He versus LN2 cooled divertor. The sc-He pumped divertor necessitated total electron fuelling rates of 1–2 $\times$ 10^{23} electrons/s, whereas the LN2 rates were 1–2 orders of magnitude lower. The divertor configuration was vertical inner and horizontal outer to optimize diagnostics (spectroscopy, Langmuir probes, Bolometry, thermal imaging). The pulses used here are: ramps 91284 (H sc-He), 95889 (D sc-He), 100559 (D LN2), 100166 (T LN2) and 99433 (DT 40 %/60 % LN2) with three more steady state "stepped" discharges: 91289 (H sc-He), 95883 (D sc-He) and 100170 (T LN2). Unfortunately, no DT sc-He or T sc-He were possible due to fact that one density limit pulse with sc-He pumped divertor would use up a whole day's inventory of tritium. Furthermore, the H LN2 was not performed due to time and programmatic constraints.

The aim of this paper is to investigate apparent dependencies on detachment on the isotope used in these density limit ramped pulsesa and to expand upon the earlier but less complete (H-D) comparision of Groth [1] Firstly, through the investigation of the B-α (electronic level n-n′ = 3–2) and B-γ (5–2) emission and their ratio which, in the past [2], has been a reasonable marker of detachment in L-mode during JET's carbon and beryllium phases (pre-2011) and, secondarily, in the behaviour of the LOS-avg electron density from the 8–2 transition (<n_e,

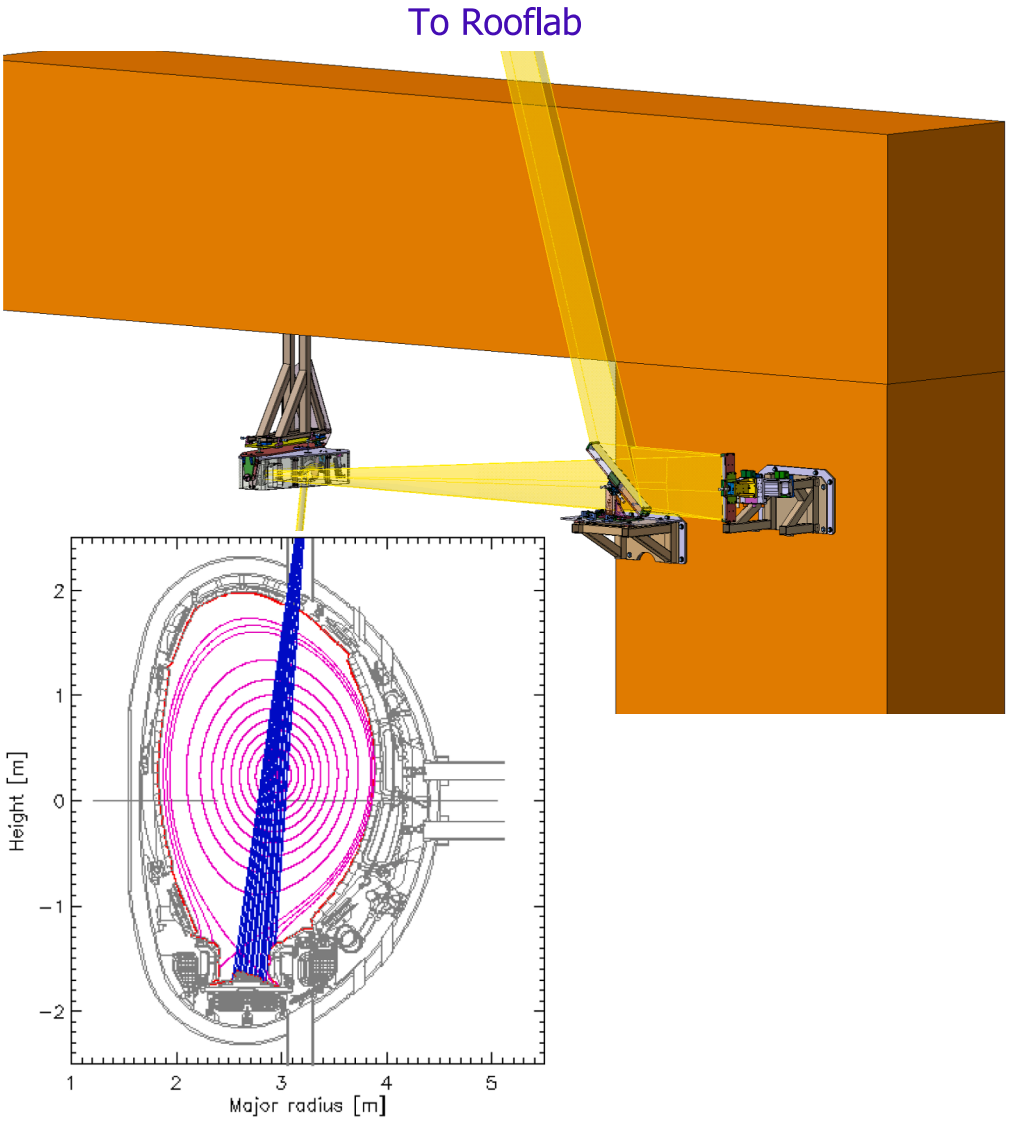

Fig. 1. Schematic of the mirror-link optical path with plasma cross-section showing the viewing geometry.

$_{Stark8\text{-}2}$>) and temperature profiles measured across the outer divertor target (<$T_{e,cont}$>).

Diagnostics

This paper used three of JET's many diagnostics for this investigation: the interferometer system described here [7], Langmuir probes [8] and the near-UV to near-IR mirror-link spectroscopy system described in [4,5] which consists of two medium resolution spectrometers, two lower resolution systems and two "fast" (0.5–1 msec frame-rate) filter cameras with Balmer-α and Balmer-© filters. The <$n_{e,Stark8\text{-}2}$> and <$T_{e,cont}$> were taken from the near-UV medium resolution system to simplify the analysis by measuring both on the same spectrometer albeit with slightly less accuracy in <$n_{e,Stark}$> than the visible spectrometer (higher resolution grating and 6–2 transition). Fig. 1 is a schematic of the 37 m optical path with example of the viewing area in the JET cross-section. The spectrometers and filter cameras are absolute intensity calibrated using an in-vessel integrating sphere. Fig. 2 shows the spectrometers approximate lines of sight and Fig. 3 compares the view of the horizontal target plate of the filter cameras against the spectrometers: this comparison is performed via plasma measurements for the filter cameras (top/A) and for one of the spectrometers set to zero wavelength and wide-open slits using the in vessel inspection lights to illuminate the divertor tiles. These spectrometers view the outer target region (tile-5) well past (inboard and outboard) of the actual target plate; however, the filter cameras exhibit vignetting on the inboard and can only see 1/3 of the inner most stack (A in the figure) of the horizontal.

Method

The edge line-average electron density, <$n_{e,edge}$>, inferred from interferometry, was used as a proxy for the electron density at the last closed flux surface at the outer midplane to provide a normalisation of the ramp rate. This signal is the outermost vertical channel of JET's interferometer, KG1. To plot all signals against <$n_{e,edge}$>, the signals were linearly interpolated onto the slowest time vector (for B-α/γ ratio this is B-γ, later for the <$n_{e,Stark8\text{-}2}$>/<$T_{e,cont}$>, the spectroscopically obtained values are slowest).

Additionally, to localise the investigation to the strike-point area, the signals were averaged in the poloidal radius to the area encompassed by the peak emission at the onset of the density ramp. For the B-a/g ratio, this was determined for each pulse with a half-width about the peak of 5 cm. Other half-widths were investigated ('full' outer target, 10 cm and 2 cm). The full outer target was quickly contaminated by the radiation that forms near the x-point at full detachment. Averaging over 10 cm was less affected but averaging over 2.5 cm was too narrow to capture most of the peak emission drift towards the x-point. For <$n_{e,Stark}$>, which has much lower spatial resolution, the two LOS at the peak were used and selected for each pulse. The same peaks were used for the <$T_{e,cont}$>.

Results

Consider first the Balmer line intensity results from the filter cameras. D sc-He (95889) B-α ramps faster (versus <$n_{e,edge}$>) than other pulses and reaches a higher final intensity (counterintuitive to its pumping). H sc-He (91284) B-α ramps similarly to the LN2 cases but reaches and exceeds the D sc-He B-α intensity, contrary to what may be expected for the much better pumping of sc-He. Fig. 4 shows $I_{sat,outer}$, B-α, B-γ and the ratio versus <$n_{e,edge}$>. The faster ramp in D sc-He B-α is likely due to the larger and ramped fuelling rate, however, H sc-He fuelling does not exhibit much different behaviour to the D sc-He fuelling. B-γ displays similar ramp slope behaviour but D sc-He begins to ramp earlier in in <$n_{e,edge}$>. The plot of the B-α/B-γ ratio displays a clear separation between sc-He and LN2 at high <$n_{e,edge}$>. In the ramp phase, the ratio has similar ramp rates, with some delay, for the LN2 pulses. However, adding 'stepped' pulse data shows that the data is distributed about the ramped case, implying that the ramp rate of the electron density is not the root cause for the discrepancy between the pumped and unpumped configurations. Errors bars were propagated from calibration, photon statistics and the spatial averaging process; these errors are on the order of 2–3 % after averaging.

Divertor electron density from Stark broadening:

The standard Balmer transition is usually the 6–2 at medium resolution (1200 l/mm grating 0.75 m imaging spectrometer). To simplify analysis and remove instrumental differences in alignment, the lower resolution near-UV system was used to obtain LOS-avg $n_{e,stark}$ and $T_{e,cont}$. Furthermore, the medium resolution spectrometer was used for other

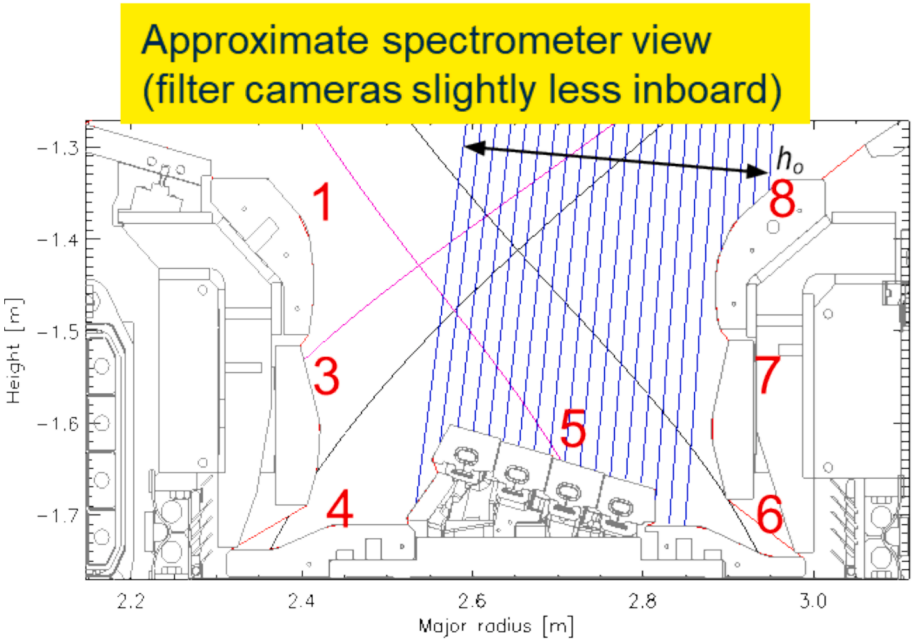

Fig. 2. Divertor view of the spectroscopy lines of sight on the divertor with a V5 magnetic configuration strike point and x-point shown. Aligning to Fig. 3: the radial stacks are on the tile labelled 5 and stack A is directly above the 2.5 m marker, stack D is above 2.8 m.

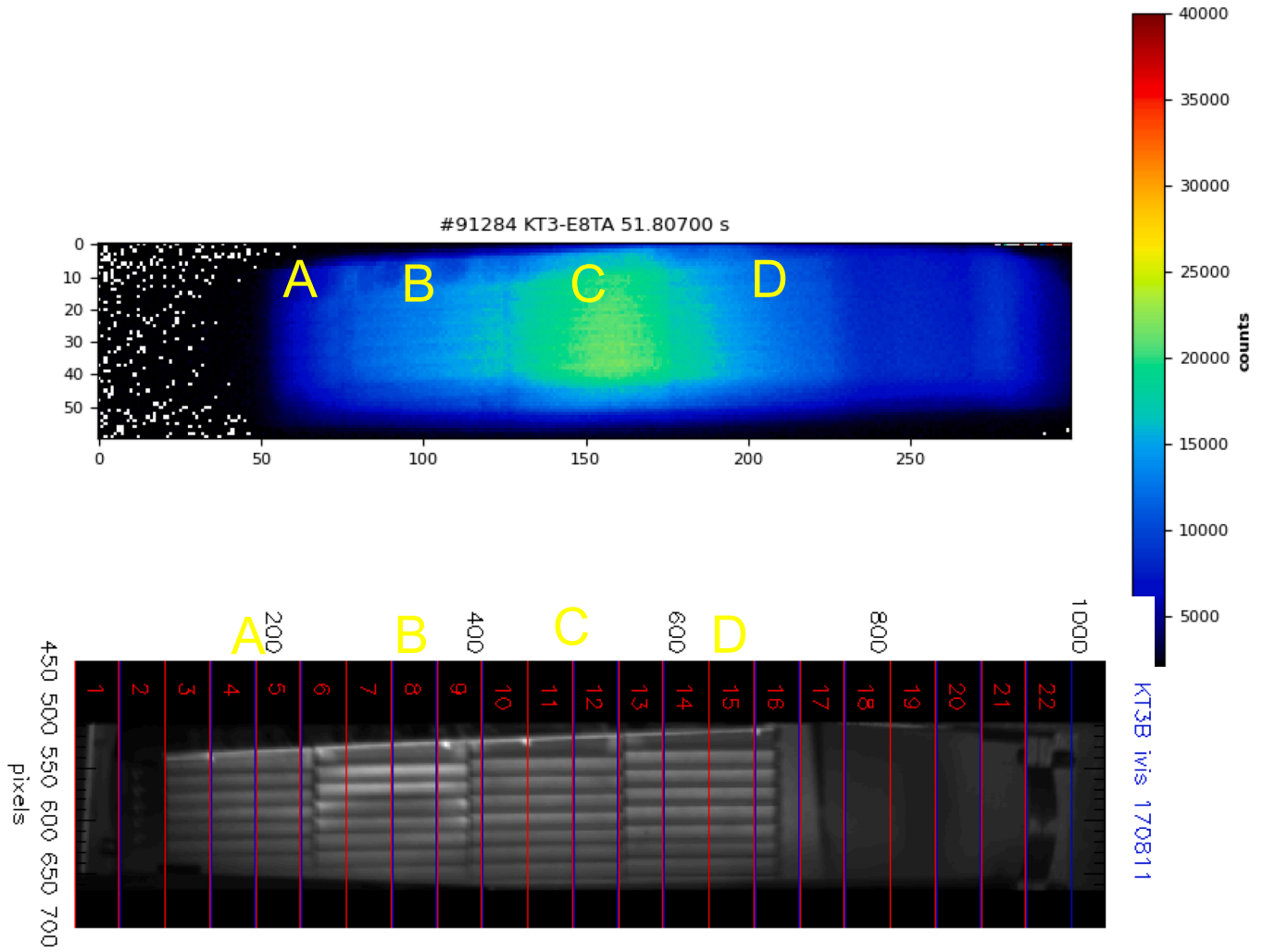

Fig. 3. Comparison of imaging field of view between the fast filter cameras (Ha camera shown on top) and the visible spectrometer leg with slits wide open and wavelength set to zero. This shows the fast cameras cannot see as far inboard as the spectrometer systems due to a Newtonian telescope misalignment that was not corrected.

measurements on a few of the pulses. To ensure the $n_{e,stark}$ from the 8–2 transition, measured with the lower resolution grating, produces similar $n_{e,stark}$ profiles (magnitude and shape) to the 6–2 using the higher resolution grating, they were compared on shots when both were available. The higher resolution 6–2 and lower resolution 7–2 and 8–2 transitions showed similar behaviour with only slight variations in magnitude due to the inaccuracies of the parameterised Stark broadening for the transitions and the lower resolution of the measurements for the 7–2 and 8–2 transitions [9].

From the peak average, the rollover electron density for the 8–2 transition, shown in Fig. 5A, occurs at similar values of $<n_{e,edge}>$ for all pulses, however, as shown in Table 1, the peak value in $<n_{e,stark\ 8\text{-}2}>$ varies between 3.2×10^{20} m^{-3} and 4.4×10^{20} m^{-3}. This plot shows some variation in $<n_{e,stark\ 8\text{-}2}>$ rollover with H sc-He being lowest and T LN2 having the highest rollover. D sc-He and D LN2 are very close to the same value. Here might be the largest isotope effect. Errors were propagated from calibration and photon statistics thru the fitting and then spatial averaging; these errors are shown in the figure.

In the space $<n_{e,stark\ 8\text{-}2}>$ vs. $<n_{e,edge}>$, H (LN2) is an outlier similar to I_{sat} vs. $<n_{e,edge}>$. There is some indication of isotope separation in the peak value of $<n_{e,stark\ 8\text{-}2}>$ at the strike point. Error analysis show that the variation of D sc-He, D LN2, T LN2 and DT LN2 is significant. The peaks of D sc-He and D LN2 are very close suggesting that the influence of pumping vs unpumped is limited. Unexplained is the H sc-He being so far from the other curves. As expected, the $<n_{e,stark\ 8\text{-}2}>$ rollover ($\sim$3.0–3.3 $\times$ 10^{20} m^{-3}) and the I_{sat} rollover ($\sim$2.6 $\times$ 10^{20} m^{-3}) are significantly different [3].

Electron temperature from the Balmer-continuum:

In Fig. 5B, the peak averaged electron temperature from the continuum, $<T_{e,cont}>$ [10], is considered against $<n_{e,edge}>$ resulting in an exponential rate of decay to $\sim$1.1 eV in all pulses. The D sc-He pulse shows a greater rate of decay. This shows small variation in decay rate visually. D sc-He advanced over all others; possibly a ramp rate effect. Error propagation has been done and are shown in the figure; the largest errors in the spatially averaged Te are about 0.05 eV (Errors after rollover in unaveraged strike point line of sight are about 0.1 eV). The $<T_{e,cont}>$ used here is only the continuum step, not the low wavelength continuum which is more sensitive at low temperatures and is likely below 1 eV [9]. Despite some small variation, each pulse reaches $\sim$1.1 eV around 3.2×10^{19} m^{-3}.

When looking at the pressure proxy, $<n_{e,stark\ 8\text{-}2}>^{*}<T_{e,cont}>$ as show in Fig. 5C, the isotope separation becomes clear and anomalies at least after I_{sat} rollover are not present. This shows probably the clearest separation by isotope after I_{sat} rollover without anomalies (T → DT → D → H with D sc-He and D LN2 nearly matching). There is a clear distinction between T/DT, D and H and even D sc-He and D LN2 match closely.

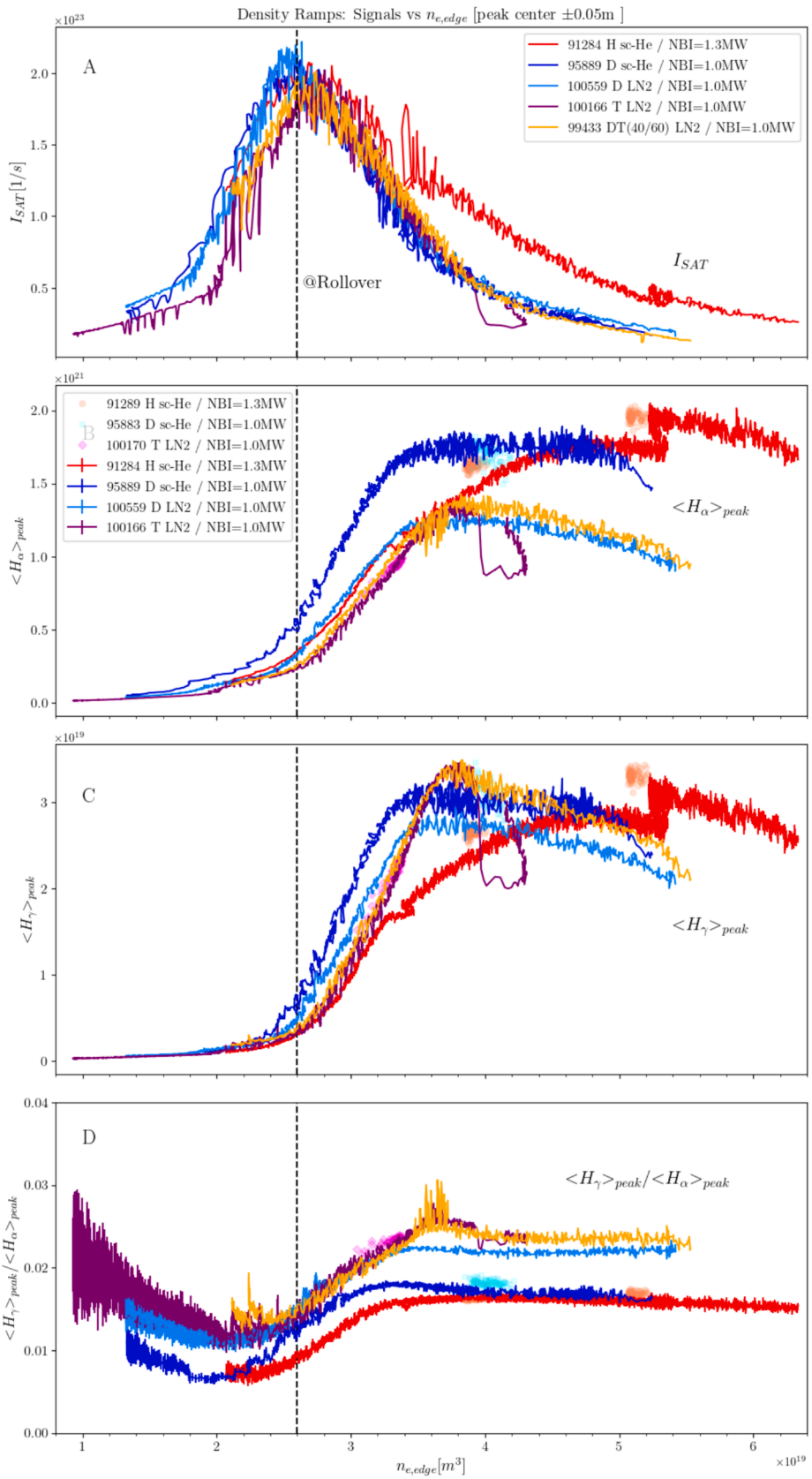

Fig. 4. $I_{sat,outer}$ (A), peak averaged Balmer-α (B) and Balmer-γ (C) and their ratio (D) versus $<n_{e,edge}>$. Units for the emission (panel B and C) are photons/m^{-2}/steradian/second. Color code for the pulses shown in Fig. 5 legend for the ramped pulses; the stepped pulses are shown in coral (91289 H sc-He), aqua (95883 D sc-He) and fuchsia (100170T LN2). The stepped results are overlap the ramped data supporting the premise that ramp rate is not a factor.

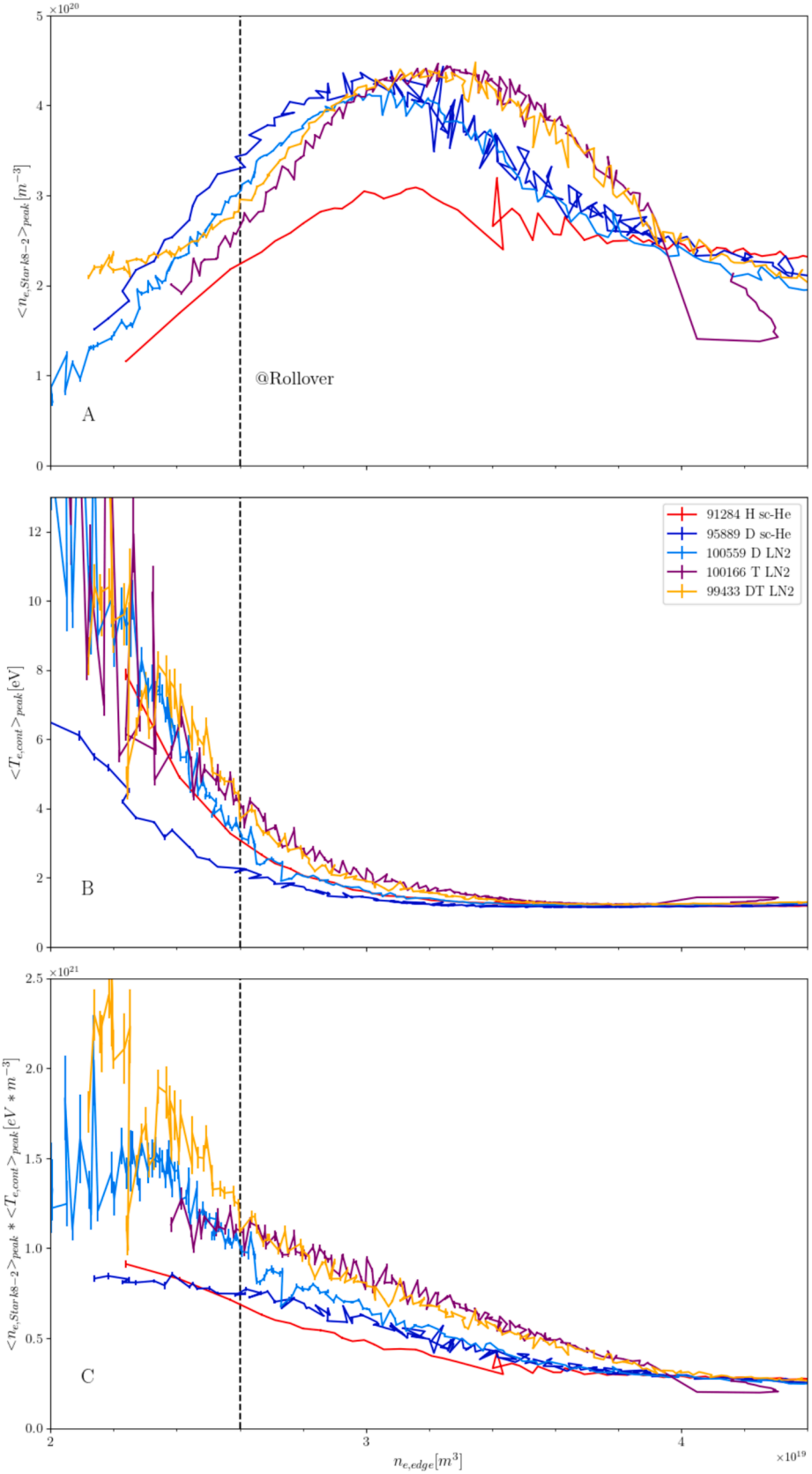

Fig. 5. $<n_{e,stark\ 8\text{-}2}>$ versus $<n_{e,edge}>$ (A) shows some variation in $<n_{e,stark\ 8\text{-}2}>$ rollover with H sc-He being lowest and T LN2 having the highest rollover. D sc-He and D LN2 are very close to the same value. Here might be the largest isotope effect; if significant. $<T_{e,cont}>$ versus $<n_{e,edge}>$ (B) show small variation in decay rate visually. D sc-He advanced over all others; possibly a ramp rate effect. The pressure proxy $<n_{e,stark\ 8\text{-}2}>*<T_{e,cont}>$ (C) shows probably the clearest separation by isotope after I_{sat} rollover without anomalies (T → DT → D → H with D sc-He and D LN2 nearly matching).

Table 1
Rollover edge electron density for each density ramp pulse.

pulse	Ion (pump)	Rollover electron density [m-3]
91284	H (sc-He)	3.20E+20
95889	D (sc-He)	4.30E+20
100559	D (LN2)	4.20E+20
100166	T (LN2)	4.40E+20
99433	DT(LN2)	4.40E+20

Summary

The 1D view of detachment utilising the average along the strike point tile is complicated by the presence of the x-point radiator that grows as complete detachment is reached. This problem is solved by taking an average around the initial peak emission at the outer strike point; by taking this spatial region on a pulse-by-pulse basis and transition (B-α and B-γ), minor differences in spatial calibration between pulses are removed. It does, however, presuppose that the two transitions peak in the same poloidal location in the divertor.

For Lines-of-sight around the strike point, the Isotope/Pumping scan resolves, in B-α/B-γ Ratio space, to a difference in pumping. However, in $<n_{e,stark}>$ vs $<n_{e,edge}>$ space, H sc-He is an outlier and there is a likely isotope dependence between D, DT and T. In $<T_{e,cont}>$ vs $<n_{e,edge}>$, D sc-He is an anomaly, and there may be an isotope effect on the decay rates. For both, $<n_{e,stark}>$ and $<T_{e,cont}>$ vs $<n_{e,edge}>$, error propagation shows that the differences are significant. Further work is intended to perform fits to this Te and pressure data.

B-γ, $<n_{e,stark}>$, and $<T_{e,cont}>$ all show broadening and shift towards the x-point as the ramp progresses. However, B-α does not show this but does show symmetrisation in spatial profile as $<n_{e,edge}>$ increases and detachment progresses.

Density step pulses were performed to remove the differences in density ramp rate. The density step data mapped well onto the ramp data which implies that the ramp rate has a minor effect.

CRediT authorship contribution statement

A.G. Meigs: Writing – original draft, Visualization, Validation, Software, Methodology, Investigation, Formal analysis, Data curation. **M. Groth:** Writing – review & editing, Visualization, Methodology, Investigation, Conceptualization. **V.-P. Rikala:** Writing – review & editing, Visualization, Methodology, Investigation, Conceptualization. **B. Lomanowski:** Writing – review & editing, Software, Methodology, Investigation, Formal analysis. **N. Vianello:** Supervision, Project administration, Funding acquisition. **M. Wischmeier:** Supervision, Project administration, Funding acquisition.

Declaration of competing interest

The authors declare that they have no known competing financial interests or personal relationships that could have appeared to influence the work reported in this paper.

Acknowledgements

This work has been carried out within the framework of the EUROfusion Consortium, funded by the European Union via the Euratom Research and Training Programme (Grant Agreement No 101052200 — EUROfusion). Views and opinions expressed are however those of the author(s) only and do not necessarily reflect those of the European Union or the European Commission. Neither the European Union nor the European Commission can be held responsible for them.

Data availability

Data will be made available on request.

References

[1] M. Groth, V. Solokha, S. Aleiferis, S. Brezinsek, M. Brix, I.S. Carvalho, P. Carvalho, G. Corrigan, D. Harting, N. Horsten, I. Jepu, J. Karhunen, K. Kirov, B. Lomanowski, K.D. Lawson, C. Lowry, A.G. Meigs, S. Menmuir, E. Pawelec, T. Pereira, A. Shaw, S. Silburn, B. Thomas, S. Wiesen, P. Börner, D. Borodin, S. Jachmich, D. Reiter, G. Sergienko, Z. Stancar, B. Viola, P. Beaumont, J. Bernardo, I. Coffey, N. J. Conway, E. de la Luna, D. Douai, C. Giroud, J. Hillesheim, L. Horvath, A. Huber, P. Lomas, C.F. Maggi, M. Maslov, C. Perez von Thun, S. Scully, N. Vianello, M. Wischmeier, Characterisation of divertor detachment onset in JET-ILW hydrogen, deuterium, tritium and deuterium–tritium low-confinement mode plasmas, Nucl. Mater. Energy 34 (2023) 101345, https://doi.org/10.1016/j.nme.2022.101345.

[2] G.M. McCracken, M.F. Stamp, R.D. Monk, A.G. Meigs, J. Lingertat, R. Prentice, A. Starling, R.J. Smith, A. Tabasso, Evidence for volume recombination in JET detached divertor plasmas, Nucl. Fusion 38 (1998) 619, https://doi.org/10.1088/0029-5515/38/4/311.

[3] M. Groth et al., IAEA-Fusion Energy Conference 2023.

[4] A. Meigs, M. Stamp, R Igreja, S. Sanders, P. Heesterman, JET-EFDA Contributors; Enhancement of JET's mirror-link near-ultraviolet to near-infrared divertor spectroscopy system, *Rev. Sci. Instrum.* 81(10) (2010) 10E532. Doi: 10.1063/1.3502322.

[5] B. A. Lomanowski, A. G. Meigs, N. J. Conway, K.-D. Zastrow, R. M. Sharples, P. Heesterman, D. Kinna, JET EFDA Contributors; Enhanced visible and near-infrared capabilities of the JET mirror-linked divertor spectroscopy system, *Rev. Sci. Instrum.* 85(11) (2014) 11E432. Doi: 10.1063/1.4893426.

[6] A.W. Leonard, Plasma detachment in divertor tokamaks, Plasma Phys. Controlled Fusion 60 (4) (2018) 044001, https://doi.org/10.1088/1361-6587/aaa7a9.

[7] A. Boboc, C. Gil, P. Pastor, P. Spuig, T. Edlington, S. Dorling, JET-EFDA Contributors Upgrade of the JET far infrared interferometer diagnostic, Rev. Sci. Instrum. 83 (2012) 10E341, https://doi.org/10.1063/1.4737420.

[8] R.D. Monk, Langmuir probe measurements in the divertor plasma of the JET tokamak, United Kingdom, N. p., 1996. Web.

[9] B.A. Lomanowski, et al., Nucl. Fusion 55 (2015) 123028, https://doi.org/10.1088/0029-5515/55/12/123028.

[10] B. Lomanowski, et al., Plasma Phys. Control. Fusion 62 (2020) 065006, https://doi.org/10.1088/1361-6587/ab7432.